



A Data-constrained Analysis for Joule Heating as a Solar Active Region Atmosphere Heating Mechanism. I. Sunspot Umbral Light Bridge

M. S. Yalim¹ , M. Frisse¹ , C. Beck² , D. P. Choudhary³ , A. Prasad⁴ , S. S. Nayak¹ , and G. P. Zank^{1,5}

¹Center for Space Plasma and Aeronomic Research, The University of Alabama in Huntsville, Huntsville, AL 35805, USA; msy0002@uah.edu

²National Solar Observatory (NSO), Boulder, CO 80303, USA

³Department of Physics and Astronomy, California State University, Northridge (CSUN), Northridge, CA 91330-8268, USA

⁴Roseland Centre for Solar Physics, University of Oslo, Blindern NO-0315, Oslo, Norway

⁵Department of Space Science, The University of Alabama in Huntsville, Huntsville, AL 35805, USA

Received 2023 November 13; revised 2024 June 29; accepted 2024 July 1; published 2024 September 19

Abstract

Understanding the mechanisms underlying the heating of the solar atmosphere is a fundamental problem in solar physics. The lower atmosphere of the Sun (i.e., photosphere and chromosphere) is composed of weakly ionized plasma. This results in anisotropic dissipation of electric currents by Coulomb and Cowling resistivities. Joule heating due to dissipation of currents perpendicular to the magnetic field by Cowling resistivity has been demonstrated to be the main mechanism for the heating of a sunspot umbral light bridge located in NOAA AR 12002 on 2014 March 13. Here, we focus on the same target region and demonstrate the importance of further constraining our Joule heating model using observational data in addition to magnetic field, namely plasma temperature calculated from the inversion of spectroscopic data obtained from the Interferometric BI-dimensional Spectrometer instrument of the ground-based Dunn Solar Telescope. As a parameter in our analysis, temperature is demonstrated to have the highest sensitivity after magnetic field. We show that the heating of the light bridge is a highly dynamic event that necessitates utilization of 3D spatially resolved observational data for temperature rather than a 1D temperature stratification based on theoretical/semiempirical solar atmosphere models. Our improved data-constrained analysis using spatially resolved temperatures shows that the entire light bridge is heated by the proposed mechanism, and yields heating rate values that are consistent with our previous study.

Unified Astronomy Thesaurus concepts: [Solar chromosphere \(1479\)](#); [Solar chromospheric heating \(1987\)](#); [Solar active region magnetic fields \(1975\)](#)

1. Introduction

A fundamental problem in solar physics is to determine the physical processes that maintain the thermal structure of the solar atmosphere (Narain & Ulmschneider 1996). Various mechanisms have been proposed to account for the thermal structure and heating of the solar atmosphere that contributes to the remarkable temperature increase from ~ 5000 K in the photosphere to ~ 1 million K in the corona. In this paper, we discuss Joule heating due to the dissipation of electric currents by magnetic resistivity, namely Cowling resistivity (Cowling 1957), as a heating mechanism of the lower solar atmosphere, namely the solar chromosphere.

Energy transfer in the chromosphere can be attributed to mechanisms such as Alfvén waves (van Ballegoijen et al. 2011; Sakae & Shibata 2020), nanoflares (Priest et al. 2018; Syntelis & Priest 2020), Ellerman bombs (EBs) (Rutten 2016; Chen et al. 2019), spicules (De Pontieu et al. 2009; Beck et al. 2016), and magneto-acoustic shocks (De Pontieu et al. 2015). Ulmschneider et al. (1978) and Kalkofen (2007) suggested that the heating of the chromosphere is due to the dissipation of acoustic waves. However, Athay & Holzer (1982) and Beck et al. (2009, 2012) questioned this last mechanism.

Another candidate to heat the solar chromosphere is resistive ohmic dissipation (Parker 1983; Tritschler et al. 2008). The plasma in the chromosphere is weakly ionized, which allows ions, neutrals,

and electrons to coexist. This results in anisotropic dissipation of electric currents by Coulomb and Cowling resistivities in directions parallel and perpendicular to magnetic field lines, respectively. Cowling resistivity follows the interactions between ions and neutrals. It is a function of plasma bulk density, temperature, and magnetic field, as well as ion and electron number densities. The Joule heating mechanism that we focus on results from the dissipation of electric currents due to Cowling resistivity (see Section 2.1). This mechanism is represented by the generalized Ohm's law as a function of Cowling resistivity and electric current perpendicular to the magnetic field.

We perform a data-constrained analysis (Yalim et al. 2020, 2023; Louis et al. 2021) to calculate Cowling resistivity and the resulting Joule heating rate in a solar active region atmosphere. In this analysis, we can obtain the stratified bulk plasma, ion and electron number densities, and temperature profiles from the tabulated data of five different theoretical/semiempirical solar atmosphere models: the Maltby M model (Maltby et al. 1986) for sunspot umbrae, the Ding & Fang model (Ding & Fang 1989) for sunspot penumbrae, the VAL C model (Vernazza et al. 1981) and the Harvard-Smithsonian Reference Atmosphere (HSRA) model (Gingerich et al. 1971) for quiet Sun, and the VAL F model (Vernazza et al. 1981) for bright filament networks. Additionally, we compute the magnetic field in the chromosphere by applying a non-force-free field (NFFF) magnetic field extrapolation technique (Hu & Dasgupta 2008; Hu et al. 2008, 2010) to the photospheric vector magnetic field data observed by the Helioseismic and Magnetic Imager (HMI, Schou et al. 2012) magnetogram onboard Solar Dynamics Observatory (SDO, Pesnell et al. 2012).



Original content from this work may be used under the terms of the [Creative Commons Attribution 4.0 licence](#). Any further distribution of this work must maintain attribution to the author(s) and the title of the work, journal citation and DOI.

In this paper, we show how we also obtain the temperature from observations in order to further constrain our data analysis using observational data, and hence decrease its reliance on the tabulated data from static solar atmosphere models. For this purpose, we perform a thermal inversion of spectroscopic data obtained by the Interferometric BI-dimensional Spectrometer (IBIS) instrument (Cavallini 2006) at the ground-based Dunn Solar Telescope (DST).

The occurrence of dynamic phenomena in the chromosphere and transition region has been attributed to plasma heating by the formation of current sheets when a discontinuity in the 3D magnetic field arises (Solanki et al. 2003; Bahaouddin et al. 2021). We focus on discontinuities in the magnetic field topology that produce electric currents that can heat the plasma in those regions by dissipation through the Cowling resistivity. Such currents can occur at all locations with strong gradients in the magnetic field strength or orientation. For example, these conditions are prevalent near light bridges (LBs) inside sunspot umbrae, for magnetic flux emergence into a field-free or magnetic environment, near polarity inversion lines, or near magnetic reconnection sites like EBs. Here, we analyze Joule heating in a sunspot umbral LB in NOAA AR 12002 on 2014 March 13.

Section 2 gives a brief overview of our data-constrained analysis to calculate Joule heating in the chromosphere. Section 3 presents our analysis results for a sunspot umbral LB and discussions. Finally, Section 4 lists our conclusions.

2. Data-constrained Analysis

2.1. Calculation of Cowling Resistivity and Joule Heating Rate

Cowling resistivity of a nonstationary plasma can be significantly increased owing to ion-acceleration by Ampère's force (Cowling 1957). The resulting high ion velocities make the collisions between ion and neutral particles very effective. From the perspective of energy balance in the weakly ionized chromosphere, Cowling resistivity leads to additional dissipation of electric currents perpendicular to the magnetic field due to ion-neutral interaction resulting in Joule heating that is several orders of magnitude larger compared to the case of a fully ionized plasma (Khomenko 2017), in which Coulomb resistivity dominates (see the Cowling and Coulomb resistivity and their corresponding Joule heating profiles in Figure 3 of Yalim et al. 2020). For this reason, our main focus is on the calculation of Cowling resistivity and its associated Joule heating rate. The anisotropic dissipation of currents due to the presence of Coulomb and Cowling resistivities can be seen in the generalized Ohm's law (Leake & Arber 2006):

$$Q = (E + v \times B) \cdot J = \eta(J_{\parallel})^2 + \eta_C(J_{\perp})^2, \quad (1)$$

where Q is the Joule heating rate, E is the electric field, v is the velocity, J is the current density with components J_{\parallel} and J_{\perp} , which are parallel and perpendicular to the magnetic field B , respectively, η is the Coulomb resistivity, and η_C is the Cowling resistivity.

To calculate the Cowling resistivity, η_C , we solve the following relation between the Cowling and Coulomb resistivities:

$$\frac{\xi_n^2 B_0^2}{\alpha_n} = \eta_C - \eta, \quad (2)$$

where B_0 is the magnetic field strength; ξ_n is an estimate for the neutral fraction and is a function of plasma bulk density and temperature; α_n is a term that accounts for the collisions of neutrals with electrons and ions and is also a function of plasma bulk density and temperature; and η , which is the Coulomb resistivity, is a function of neutral, ion, and electron number densities as well as temperature. Finally, the electric current density and its components parallel and perpendicular to the magnetic field in Equation (1) are a function of the magnetic field.

The details of the model and how each parameter in Equation (2) is calculated can be found in Yalim et al. (2020).

2.2. Data

To calculate the Coulomb and Cowling resistivities, we need the magnetic field B , the plasma bulk density ρ , and temperature T , as well as the ion and electron number densities, n_i and n_e , in the chromosphere.

We determine the 3D spatial variation of T in the vicinity of the sunspot umbral LB located in NOAA AR 12002 in the chromosphere at 20:55 UT on 2014 March 13 by using the calcium inversion based on a spectral archive (CAISAR) code (Beck et al. 2013a, 2015, 2019), which inverts the spectroscopic data in the Ca II IR line at 8542 Å obtained from DST/IBIS (see also Louis et al. 2021). The inversion uses 1D stratifications and is executed on a pixel base. IBIS has a spatial sampling of 0.''1 per pixel.

We compute the 3D spatial variation of B by applying the NFFF magnetic field extrapolation technique to Spaceweather HMI active region patch (SHARP) vector magnetogram data from SDO/HMI at 20:48 UT and 21:00 UT on 2014 March 13. The pixel size of HMI is 0.''5 \approx 362 km, and the spatial resolution is 1''.

For our observations, there is no higher resolution vector magnetogram from Hinode/SP available. However, even though HMI underestimates the field strength in plage regions (Sainz Dalda 2017), the magnetic filling factor is close to 1 inside the sunspot, and the observed magnetic field and the calculated electric current values there can be mostly trusted. Moreover, considering one of the main reasons for us to use magnetograms in this study is to locate the discontinuity above the LB by extrapolating the 3D magnetic field topology using NFFF, the HMI SHARP vector magnetograms that we use serve this purpose well.

For the 1D variation of the bulk plasma density ρ , electron number density n_e , and the total hydrogen number density n_H with height above the photosphere, we use tabulated data from the Maltby M, VAL C, VAL F, Ding & Fang, and HSRA atmosphere models. We then calculate n_i from n_e and n_H .

It should be noted that we have the option to use either 1D stratified temperature profile with height above the photosphere from the tabulated model data or 3D temperature data from the inversion results of IBIS spectroscopic observations to compare the effects of the data source for temperature on our analysis results.

After calculating the Cowling resistivity, we then compute the perpendicular electric currents from the gradients of the 3D extrapolated magnetic field topology to calculate the Joule heating rate from the generalized Ohm's law as $\eta_C J_{\perp}^2$.

2.3. Note on the NFFF Magnetic Field Extrapolation Technique

The NFFF extrapolation technique used in this work was developed by Hu & Dasgupta (2008) and Hu et al. (2008, 2010). Accordingly, the magnetic field B is written as

$$B = B_1 + B_2 + B_3; \nabla \times B_i = \alpha_i B_i, \quad (3)$$

where for $i = 1, 2, 3$, each subfield B_i corresponds to a linear-force-free field (LFFF) with corresponding constants α_i . Further, without loss of generality, one can choose $\alpha_1 \neq \alpha_3$ and $\alpha_2 = 0$ making B_2 a potential field. However, unlike in the LFFF extrapolations, we do not set the values of α_i manually. Instead, an optimal pair of $\alpha = \{\alpha_1, \alpha_3\}$ is searched over a prescribed grid by the NFFF extrapolation code using an iterative trial-and-error method, which finds the pair that minimizes the average deviation between the observed (B_t) and the calculated (b_t) transverse fields on the photospheric boundary. The code tries to work with different partitions of $B_z = B_{z1} + B_{z2} + B_{z3}$ such that the effective twist creates a spatially varying twist distribution that matches the observations the best (see, e.g., Equation (13) in Mitra et al. 2018).

Regarding the effects of periodic boundaries, in order to minimize the boundary effects, we try to keep our region of interest close to the box center and apply a Hanning window that slowly puts the B_z values to zero over a range of pixels (typically 16 pixels).

The Hanning window is actually applied to the pixels near the boundary. For the current extrapolation box, the bottom boundary aspect ratio is 2:1 (i.e., 600:300 HMI pixels), so we used a (32, 16) Hanning window. The function smooths the edges of B_z to zero to ensure the validity of periodic boundary conditions by applying a cosine taper to the edges of the box by (32, 16), which are the number of elements in the taper in the x and y directions, respectively. This ensures that the values at the boundaries gradually decrease to zero, thereby avoiding discontinuities.

In comparison with the size of our extrapolation box, the LB is far from the side boundaries and only the lowest three HMI pixel heights among the 300 HMI pixel height range of the extrapolation box are of relevance for our analysis. As another example to support our argument, in Figures 4 and 5 of Prasad et al. (2018), the correlation of the transverse photospheric magnetic field, B_t , between the original magnetogram and the extrapolated field is shown. Since only B_z is directly used in the calculation of NFFF and B_t is used as a constraint to optimize the fit, a good correlation shows that we match the photospheric boundary well, and the underlying assumptions of flux-balance and periodic boundary are acceptable within the requirements of our calculations.

In this study, we prefer to use the NFFF extrapolation technique as it is especially suited to model photospheric and chromospheric magnetic fields that are not force free (Gary 2001). Additionally, the extrapolated magnetic fields by NFFF yield a J_{\perp} component, which is necessary to calculate the Joule heating rate due to the Cowling resistivity unlike the nonlinear-force-free field (NLFFF) extrapolation technique whose extrapolated magnetic fields only yield a J_{\parallel} component.

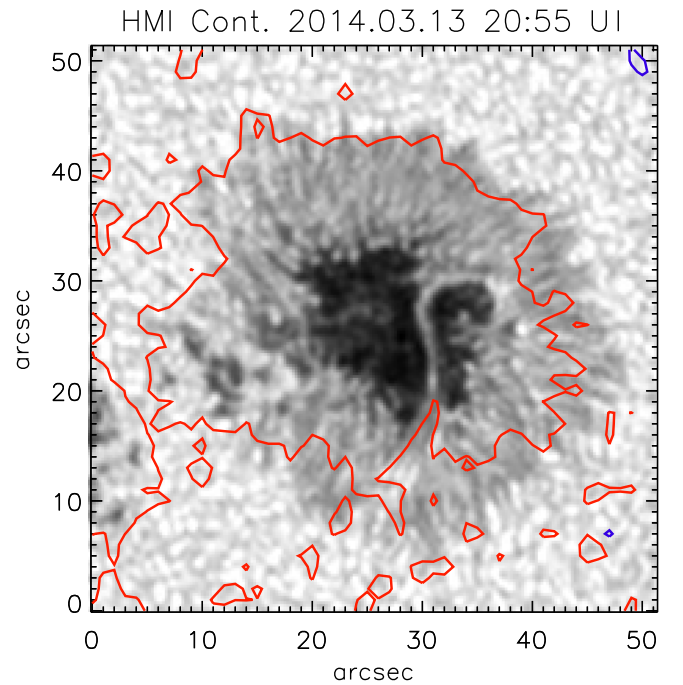


Figure 1. HMI continuum image (generated using the “Enhance” code (Baso & Ramos 2018) to improve the resolution of the HMI Continuum image) at 20:55 UT on 2014 March 13 with contours at ± 200 G (red for positive and blue for negative) for the vertical component of the magnetic field.

3. Results and Discussions

3.1. Target Structure: Sunspot Umbral Light Bridge

As a primary target structure in our analysis, we focus on a sunspot umbral LB. LBs are elongated bright structures that are usually present during the early stages of sunspot formation or the late stages of sunspot decay and can have an umbral, penumbral, or granular morphology (Louis et al. 2020) (see Figure 1). They are relatively long lived (hours to days) and relatively steady (less dynamic) structures, which make them particularly suitable for heating by our proposed Joule heating mechanism.

3.2. Incorporation of Temperature from Observations into the Data-constrained Analysis

Louis et al. (2021) demonstrated that the primary heating mechanism in a sunspot umbral LB caused by flux emergence is Joule heating due to dissipation of electric currents perpendicular to the magnetic field by the Cowling resistivity based on our data-constrained analysis that involves data from observations and solar atmosphere models. In that study, we utilized only magnetic field from observations (in particular, SDO/HMI SHARP vector magnetograms) while the remaining plasma parameters including temperature were taken as 1D profiles with respect to height above the photosphere from the tabulated data given by the Maltby M model for sunspot umbrae.

In this paper, we build upon this previous analysis by incorporating temperature from observational data instead of tabulated data from solar atmosphere models. The main reason for selecting temperature in further constraining our analysis by observational data after the magnetic field is that the Cowling resistivity, and hence the corresponding Joule heating rate,

Table 1

Sensitivity Analysis: Maximum Percentage Change in Cowling Resistivity when Temperature T or Plasma Bulk Density ρ is Modified by a Delta Factor Multiple of the Minimum Value of the Corresponding Variable Everywhere in Figure 2 (left panel) between 0 and ~ 1086 km Height Above the Photosphere

Variable	Max % Change in Cowling Resistivity	Delta factor (*min(Variable))
T	16.44	0.01
T	57.86	0.05
T	80.78	0.1
ρ	1.476	0.01
ρ	7.033	0.05
ρ	13.28	0.1

Notes. The change in Cowling resistivity is proportional to the Delta factor. The analysis is done using the Maltby M model for sunspot umbrae for all parameters except B , which is obtained from the application of NFFF extrapolation technique to the SDO/HMI SHARP data at 21:00 UT.

have temperature as the most sensitive parameter after the magnetic field. In Table 1, the results of our sensitivity analysis are presented. To determine the sensitivity, we modified the original values of T and ρ by 1%, 5%, and 10% of the minimum value of the corresponding parameter in the HMI SHARP field of view (FOV) in Figure 2 (left panel) between 0 and ~ 1086 km height above the photosphere. We then recalculated the Cowling resistivity and determined its relative change with respect to the original value. Accordingly, among the two high-sensitivity parameters other than B , which has already been calculated using observational data, the temperature T has a much higher sensitivity (i.e., the maximum percentage change in Cowling resistivity per the same Delta factor) than the plasma bulk density ρ .

Figure 2 (left panel) shows the FOV of the HMI SHARP magnetogram (outer box), which is 600×300 HMI pixels, as well as the IBIS FOV (solid box) and a smaller FOV (dashed box) zooming in on the LB, which are 194×194 and 100×100 HMI pixels, respectively. The results that we will present in this paper are based on this smaller FOV, which is shown in more detail in the right panel of the same figure.

In order to replace the tabulated temperature data with the observational temperature data in our analysis, it is necessary to ensure the consistency between the observational temperature data and the remaining plasma variables taken from the tabulated solar atmosphere model data. We have five different solar atmosphere models that model different types of regions of the solar atmosphere. In order to determine the model to use with observed temperature in our analysis, we compare the IBIS temperature data with the 1D stratified temperature variation with height above the photosphere from all five models as shown in Figure 3. We make this comparison at a representative location on the LB, which is the location where the height-averaged IBIS temperature values are maximum (see Figure 6; top-left panel) along the white line shown in Figure 2 (right panel) that crosses approximately the center of the LB.

While we used the Maltby M model in our previous analysis in Louis et al. (2021), the temperature data from IBIS that is obtained from the nonlocal thermodynamic equilibrium (NLTE) version of the CAISAR inversion code, which is more accurate than the local thermodynamic equilibrium (LTE) version of CAISAR, has the best agreement with the temperature stratification data from the VAL F model, and also from the VAL C and HSRA models within the 0–1485 km

height range above the photosphere (see Figure 3). The main reason for this agreement is that the temperature of the LB is higher than the cooler sunspot temperature, being close to the granulation temperature. We note that 1485 km is the maximum height at which we obtain IBIS temperature data from the CAISAR inversion code, which is less than the maximum height of each model atmosphere that we used.

3.3. Comparison between Solar Atmosphere Models with/without Observational Temperature

Let us first consider the variations of the Cowling resistivity and the associated Joule heating rate. Figure 4 (top row) shows the variations of the maximum values of η_C and the Joule heating rate with height above the photosphere using tabulated data including temperature from all five solar atmosphere models. Accordingly, the Cowling resistivity in the Maltby M and Ding & Fang models, which model the relatively cooler sunspot atmosphere, peaks at a lower height, and leads to larger η_C and Joule heating rate values than in the quiet-Sun/plage region models, VAL C, VAL F, and HSRA. The major reason for this grouping of models is the strong (quadratic) dependence of Cowling resistivity on the neutral fraction, ξ_n , (see Equation (2)), which becomes larger over the cooler sunspot atmosphere than in the quiet-Sun/plage regions. In addition, α_n becomes smaller over the sunspot atmosphere due to its dependence on temperature (see Equation (9) in Yalim et al. 2020), which also contributes to the increase in the η_C values calculated from the sunspot atmosphere models.

Figure 4 (bottom row) shows the variations of the maximum values of η_C and the Joule heating rate with height above the photosphere using tabulated model data or IBIS data for temperature in our analysis. For all three model selections used to calculate the Cowling resistivity, namely VAL F, VAL C, and HSRA, using the spatially resolved inversion NLTE temperature distribution from IBIS instead of the 1D tabulated temperature profile leads to Joule heating rate values that are two to three orders of magnitude larger. This result shows clearly the effect of using observational temperature data in our analysis. We should, however, note that the locations of the maximum values of η_C and the Joule heating rate are not necessarily located on the LB at each height. For this reason, we also looked into the variations of η_C and the corresponding Joule heating rate with height at a representative location in the vicinity of the center of the LB, namely the pixel on the white line where the height-averaged IBIS NLTE temperature data is maximum (see Figure 6; top-left panel). Accordingly, in Figure 5, both η_C and the associated Joule heating rate profiles have larger values up to two orders of magnitude when the IBIS temperature profile is used rather than the VAL F model temperature profile for heights above ~ 650 km. This difference between using the IBIS and VAL F model temperature profiles varies from pixel-to-pixel as discussed in Section 3.5. What does not vary is the orders of magnitude difference between the Cowling and Coulomb resistivities and their corresponding Joule heating rate profiles. In fact, this is our motivation for considering Cowling resistivity for the proposed heating mechanism rather than the Coulomb resistivity in the chromospheric heights. To give some quantitative examples from Figure 5, the Cowling and Coulomb resistivity values at 1485 km, which is the maximum geometrical height for the inverted IBIS temperature data are $1925 \Omega \text{ m}$ and $1.36 \times 10^{-3} \Omega \text{ m}$, respectively when the VAL F model temperature is used. This difference becomes an order of magnitude

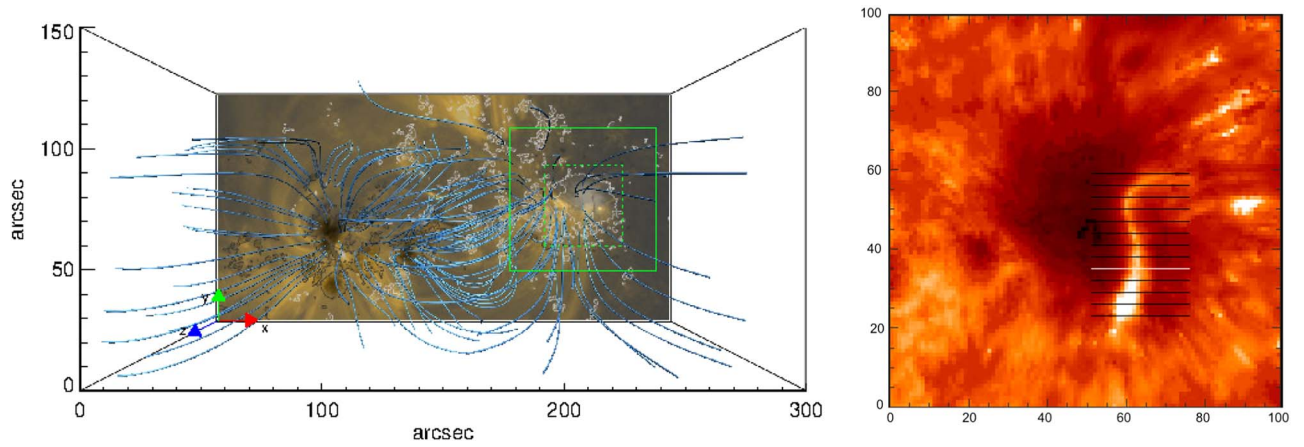


Figure 2. Left: field lines derived from the non-force-free field (NFFF) extrapolation are overlaid on a composite image of the vertical component of the magnetic field and the SDO/AIA 171 Å image for the SHARP FOV of AR 12002, which consists of 600×300 SDO/HMI pixels. The solid and dashed green squares correspond to the IBIS FOV, which consists of 194×194 SDO/HMI pixels, and the smaller FOV that zooms in on the LB and is shown in the right panel, respectively. The contours for the vertical component of the magnetic field are at ± 200 G (white for positive and black for negative). Right: local thermodynamic equilibrium (LTE) temperature distribution in the vicinity of the LB at 20:55 UT is shown at $z = 0.36$ Mm height above the photosphere. Sunspot LB in AR 12002 shown in this FOV is represented by the dashed green square in the left panel that consists of 100×100 SDO/HMI pixels. There are 13 horizontal lines that cut across the LB. In particular, we present the results of our analysis based on the white line.

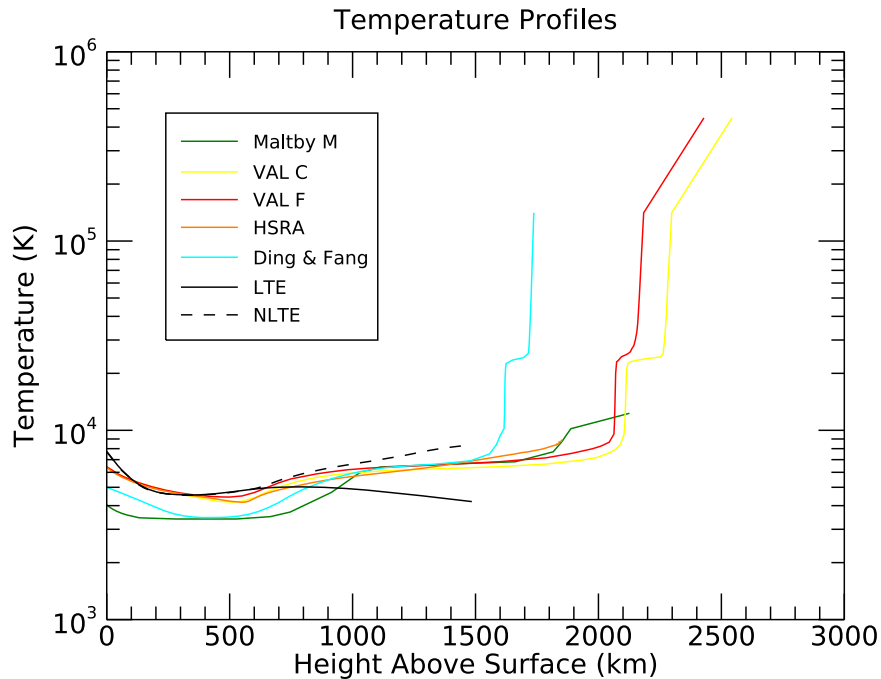


Figure 3. Temperature profiles in the chromosphere vs. height above the photosphere from the tabulated data of five solar atmosphere models are shown. The LTE and NLTE temperature profiles are obtained from an inversion of spectroscopic data from DST/IBIS at the locations where the height-averaged LTE and NLTE temperature values are maximum along the white line in Figure 2 (right panel), respectively.

larger when the IBIS temperature is used for which η_C and η values become $71,190 \Omega \text{ m}$ and $1.16 \times 10^{-3} \Omega \text{ m}$, respectively. This is also reflected in the corresponding Joule heating rate values where the dissipation of perpendicular/parallel electric currents due to Cowling/Coulomb resistivity yield 4.15 W m^{-3} and $3.14 \times 10^{-12} \text{ W m}^{-3}$, respectively, when the IBIS temperature is used versus 0.10 W m^{-3} and $9.24 \times 10^{-10} \text{ W m}^{-3}$, respectively, when the VAL F model temperature is used.

3.4. Comparison Along the White Line in Figure 2

Let us now focus specifically on the LB. Figure 6 (top-left panel) shows the horizontal variation in the LTE and NLTE

temperature data, averaged in height between 180 and 690 km above the photosphere, across the center of the LB along the white line. The bottom-left and -right panels in the same figure show the horizontal variation of the current perpendicular to the magnetic field J_{\perp} , η_C , and the Joule heating rate along the white line, all of which are averaged in height between 0 and ~ 1086 km above the photosphere. The latter height value corresponds to the height of three SDO/HMI pixels approximately. While η_C is calculated from tabulated plasma data from the VAL F model in both panels, tabulated temperature data are used in the bottom-left panel whereas the inverted temperature data from IBIS are utilized in the bottom-right panel. While the distributions of all three quantities are qualitatively similar in

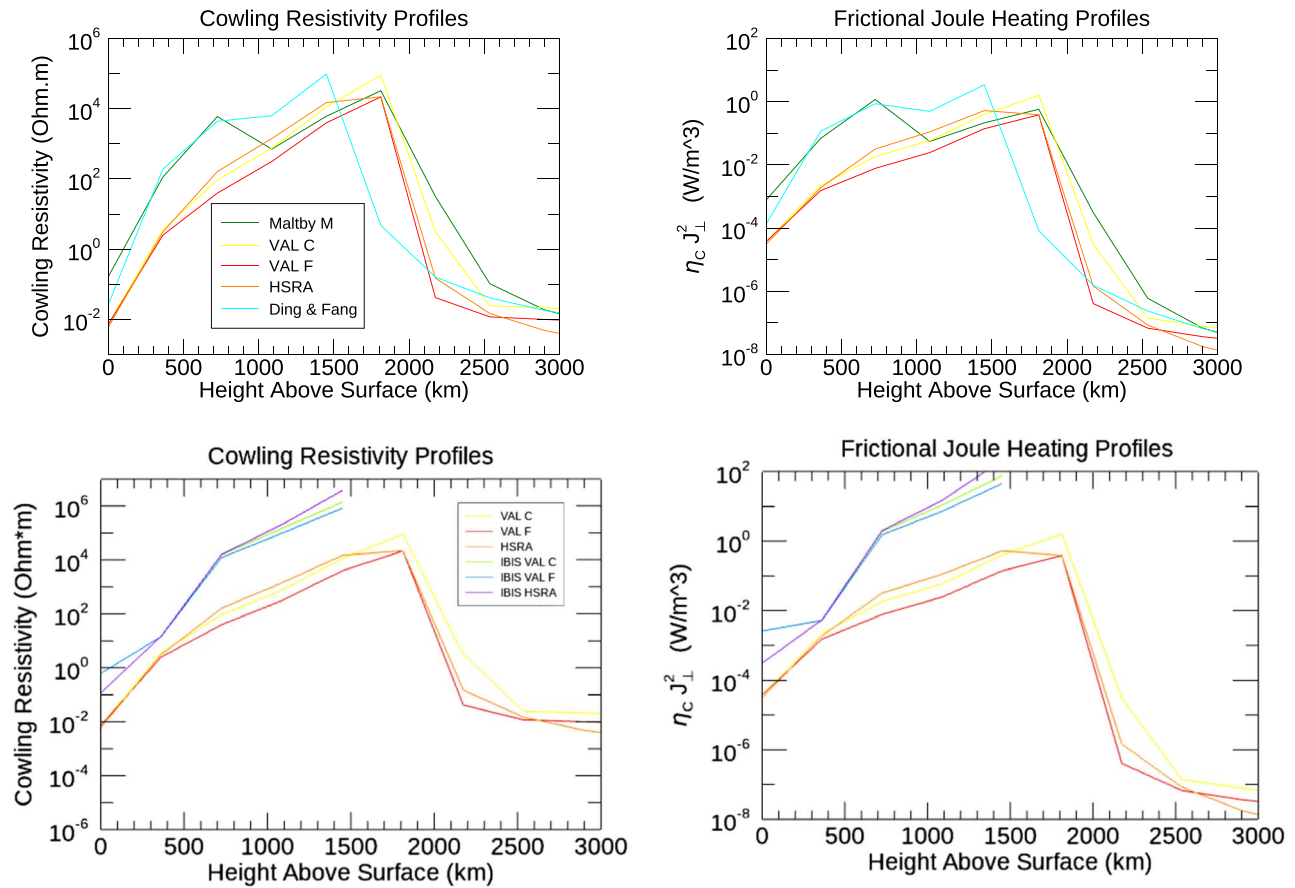


Figure 4. Top row: variation in the maximum values of (left panel) η_c and (right panel) Joule heating rate profiles with height above the photosphere, calculated from the Maltby M, VAL C, VAL F, HSRA, and Ding & Fang models. Bottom row: variation in the maximum values of (left panel) η_c and (right panel) Joule heating rate profiles with height above the photosphere, calculated from the quiet-Sun models (VAL C, VAL F, and HSRA) with temperature from either model or DST/IBIS data (NLTE). The DST/IBIS and SDO/HMI data correspond to AR 12002 at 20:55 UT and 21:00 UT, respectively.

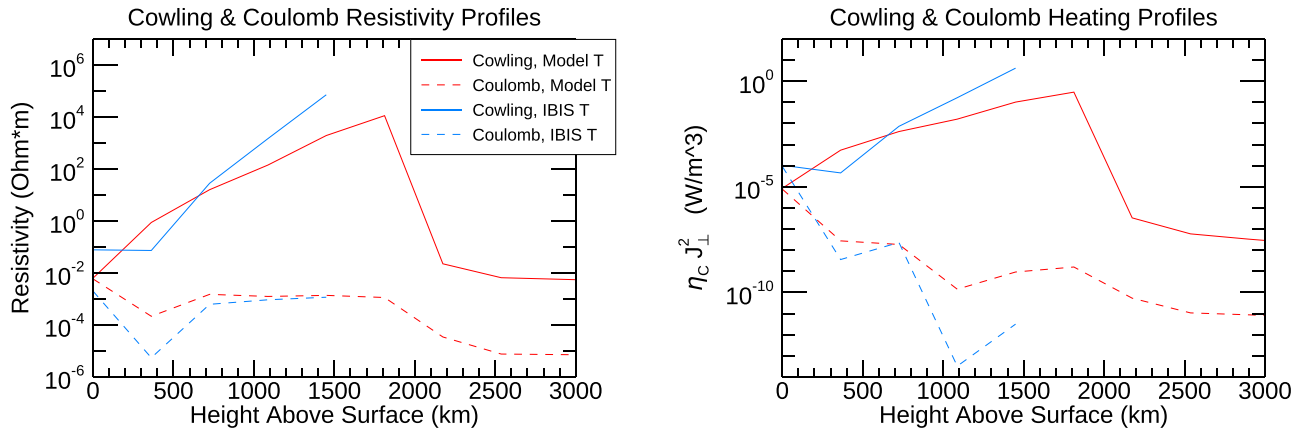


Figure 5. (Left panel) Cowling and Coulomb resistivity, and (right panel) their associated Joule heating rate profiles with VAL F model (red) and IBIS data (blue) temperature profiles in the pixel on the white line in Figure 2 where the height-averaged IBIS NLTE temperature data is maximum (see Figure 6; top-left panel).

both bottom-left and -right panels, quantitatively the maximum value of the height-averaged Joule heating rate is ~ 29 times higher when the IBIS temperature data are used. This is mainly because utilizing the spatially resolved inversion temperature data from IBIS results in an order of magnitude larger values for η_c than utilizing the 1D temperature stratification profile from the VAL F model.

To compare the results in the Figure 6 (bottom row) with a different type of model, we calculated all quantities except the

magnetic field using Maltby M, which models the sunspot umbral atmosphere in the top-right panel and is also the solar atmosphere model that we utilized in our previous analysis (Louis et al. 2021). Accordingly, the maximum height-averaged Joule heating rate value for the Maltby M model is only ~ 1.3 times larger than the Joule heating rate value for the VAL F model with IBIS temperature data. The results and the corresponding comparisons made in this figure indicate that despite the complexity of the 3D IBIS temperature data and

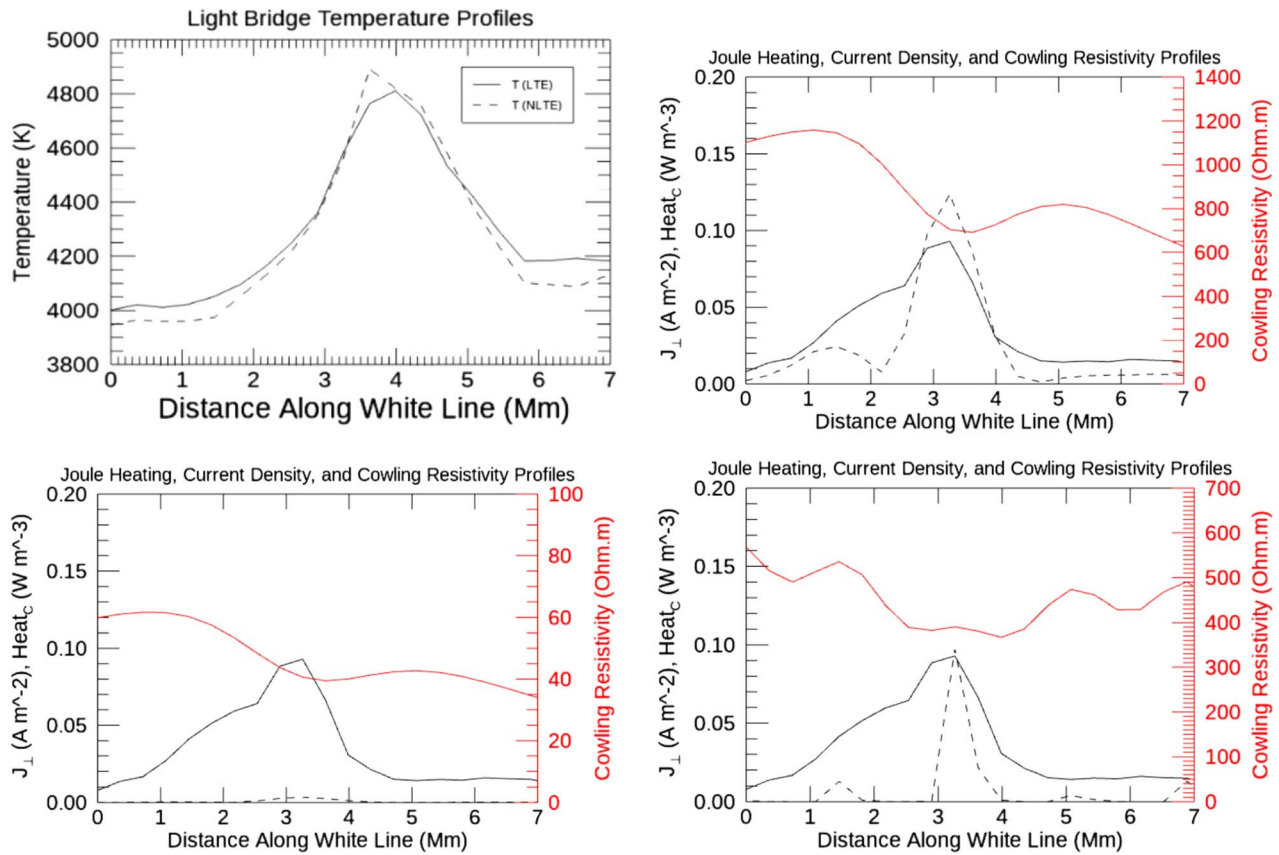


Figure 6. Top row: (left panel) horizontal variation in the LTE and NLTE temperatures from DST/IBIS data, averaged in height between 180 and 690 km above the photosphere, along the white line shown in Figure 2 (right panel) across the LB; (right panel) the Joule heating rate (dashed), J_{\perp} (solid), and η_C profiles along the white line using the Maltby M model data including the temperature. Bottom row: the Joule heating rate, J_{\perp} , and η_C profiles along the white line using (left panel) the VAL F model data including the temperature and (right panel) the VAL F model data with NLTE temperature data from inversion of spectroscopic data from DST/IBIS. All three quantities are averaged in height up to ~ 1086 km. J_{\perp} has been scaled up by a factor of 3, and the Joule heating rate has been scaled down by a factor of 2. No scaling has been applied to η_C . Gaussian smoothing has been applied to η_C with a window of two pixels for the bottom-right panel. The DST/IBIS and SDO/HMI data correspond to AR 12002 at 20:55 UT and 21:00 UT, respectively.

strong dependence of our analysis results on temperature (see Table 1), we could consistently incorporate it into our analysis and obtain a Joule heating rate distribution similar to our previously published results in Louis et al. (2021). In addition, the location of the peak of the NLTE temperature from IBIS coincides with the peak of the Joule heating rate, which supports the role of our proposed Joule heating mechanism in heating the LB. If we consider the variation of the two terms on which the Joule heating rate depends, namely η_C and J_{\perp} , we see that, while η_C makes a dip, J_{\perp} has a peak at the peak location of the NLTE temperature from IBIS. This result indicates that the presence and variation of J_{\perp} plays a major role in our proposed heating mechanism.

3.5. Dynamic (Spatially Varying) Behavior of Joule Heating

The results shown in Figure 6 were based on a height averaging of the quantities along the white line. To address how η_C and the associated Joule (ohmic) heating rate vary with height in the vicinity of the LB, Figure 7 presents the variations of these quantities at two different locations (see caption of Figure 7) in the vicinity of the LB. The highly dynamic nature of Joule heating can be clearly seen as the profiles in these locations, which are only ~ 1600 km apart from each other, are very different from each other both qualitatively and quantitatively.

Another indication of the dynamic behavior of Joule heating is apparent in its 2D variation (see Figure 8) together with the variation of its constituents η_C and J_{\perp} in the vicinity of the LB, in particular the latter within the dashed line box FOV (see Figures 9). In both Figures 8 and 9, the horizontal maps of η_C , Joule heating rate, and different components of J calculated according to the explanations in the respective figure captions are shown. We find that the perpendicular currents and the Joule heating rate are focused on the entire LB. This result holds regardless of whether the observational temperature is used or not in our analysis. Additionally, Cowling resistivity values in the LB are less than the surrounding umbra, which agrees with its 1D variation along the white line in Figure 6.

3.6. Total Joule Heating Rate of the LB with/without Observational Temperature Data

Finally, let us make a quantitative comparison of the total Joule heating rate values. We calculate this by integrating the individual Joule heating rate values at each height between 0 and ~ 1086 km at the location where the height-averaged Joule heating rate value is maximum on the LB along the white line as well as at the 13 pixels centered at the spine of the LB at each horizontal line crossing the LB covering the entire LB structure. Table 2 presents the total Joule heating rate values obtained by using tabulated plasma variable values from each

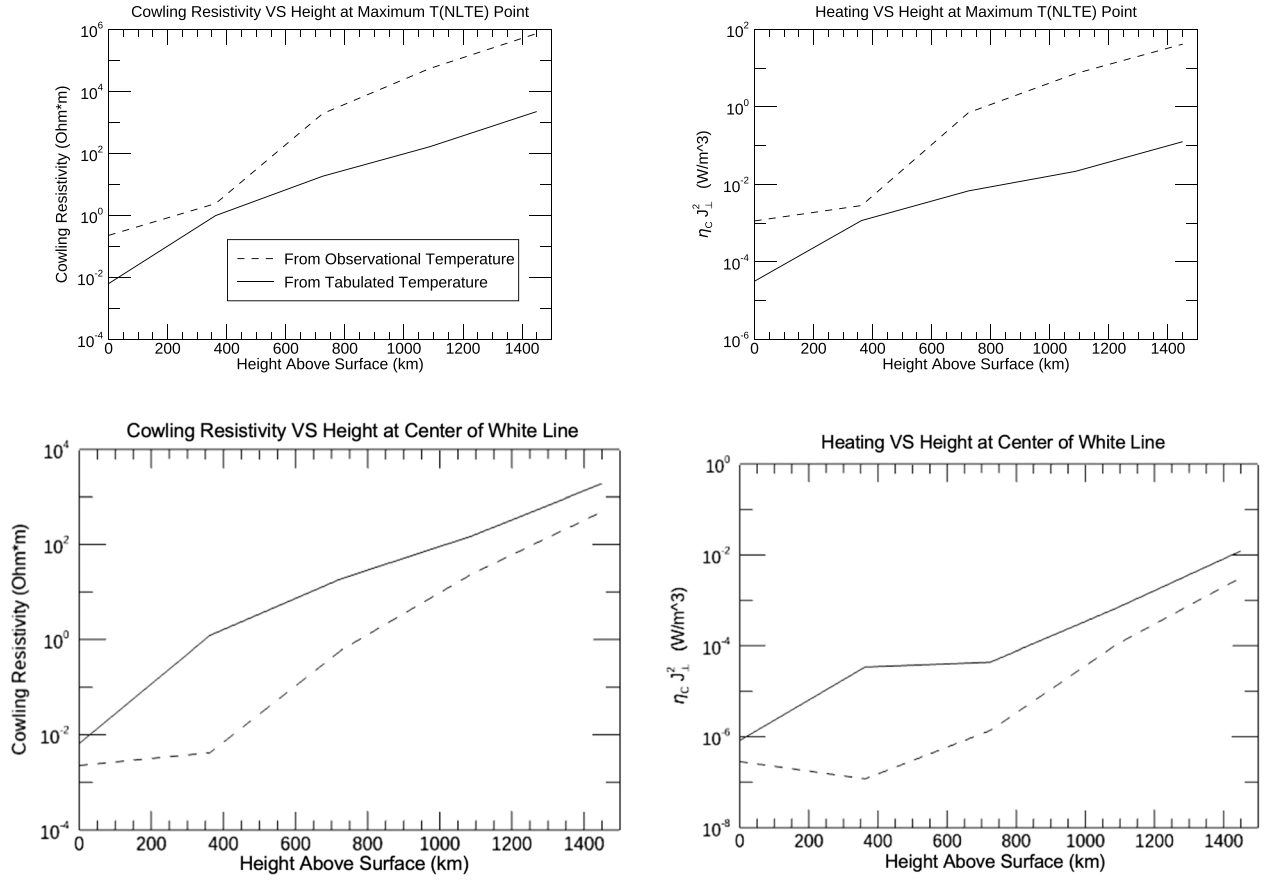


Figure 7. Top row: (left panel) η_c and (right panel) Joule heating rate variation with height at the location in the dashed line box in Figure 2 (left panel) where the DST/IBIS NLTE temperature is maximum between the heights ~ 1086 and 1448 km above the photosphere (i.e., the height of the third and fourth HMI-sized pixels above the photosphere). Bottom row: (left panel) η_c and (right panel) Joule heating rate variation with height at the center of the white line across the LB in Figure 2 (right panel).

atmosphere model and magnetic field from NFFF at two different times, namely 20:48 and 21:00 UT. As can be seen, the Joule heating rate values are consistently larger at 21:00 UT than their values at 20:48 UT for each model both at the specific location on the white line and the entire LB globally, which demonstrates that there is an ongoing heating event in the LB based on our proposed heating mechanism. This LB has previously been shown to have been formed hours before 20:48 UT (Louis et al. 2020, 2021) and remained stable and bright for hours until well after 21:00 UT (see Figures 16 and 17 in Louis et al. 2020). While we cannot exclude other heating mechanisms, the strong spatial correlation of the internal energy calculated based on the IBIS temperature stratification (Beck et al. 2013b; Rezaei & Beck 2015) with the total Joule heating rate that we showed in Figure 5 of Louis et al. (2021) strongly suggests that our proposed heating mechanism heats this LB structure between 20:48 UT and 21:00 UT. The effect of the two groups of solar atmosphere models (i.e., the cooler sunspot and warmer quiet-Sun/plage models) can also be seen in the magnitudes of the values obtained for the total Joule heating rates, with the Maltby M and Ding & Fang models giving significantly higher results (up to 40–42 times) than the VAL C, VAL F, and HSRA models at both times, both at the specific location on the white line and over the entire LB. This result is obtained when tabulated model data are used in our calculations for all five models including the 1D temperature stratification profiles. If the VAL F model is used with the 3D spatially resolved inversion IBIS

temperature data, we observe that all the total heating rate values obtained with this model/data configuration (i.e., VAL F + IBIS NLTE temperature) increase significantly and become comparable with the Maltby M and Ding & Fang model results, which are more accurate since the LB structure we are analyzing is located within the sunspot atmosphere. In other words, while utilizing the VAL F model with the tabulated model temperature in our calculations results in the lowest heating rate among all five models, by just changing the source of temperature data from tabulated model to IBIS, the accuracy of our total Joule heating rate calculations increases dramatically. Hence, once again this result shows the importance and impact of using observational data for temperature instead of tabulated data in our analysis.

Theoretical models of the solar atmosphere such as the ones we partly used in this study give average values of plasma parameters such as temperature and density. Time-dependent 3D MHD simulation results such as in Bourdin et al. (2014) or data from observations, however, may strongly deviate from the former since they take into account the dynamic evolution of the solar atmosphere. In this study, we significantly reduced the dependence of our analysis on the theoretical/semiempirical model values by using observational data for the highest two sensitive parameters in our analysis, namely magnetic field and temperature. We plan to reduce this dependence even further in our subsequent studies by incorporating more parameters from observational data. However, we also demonstrated that theoretical models when used with

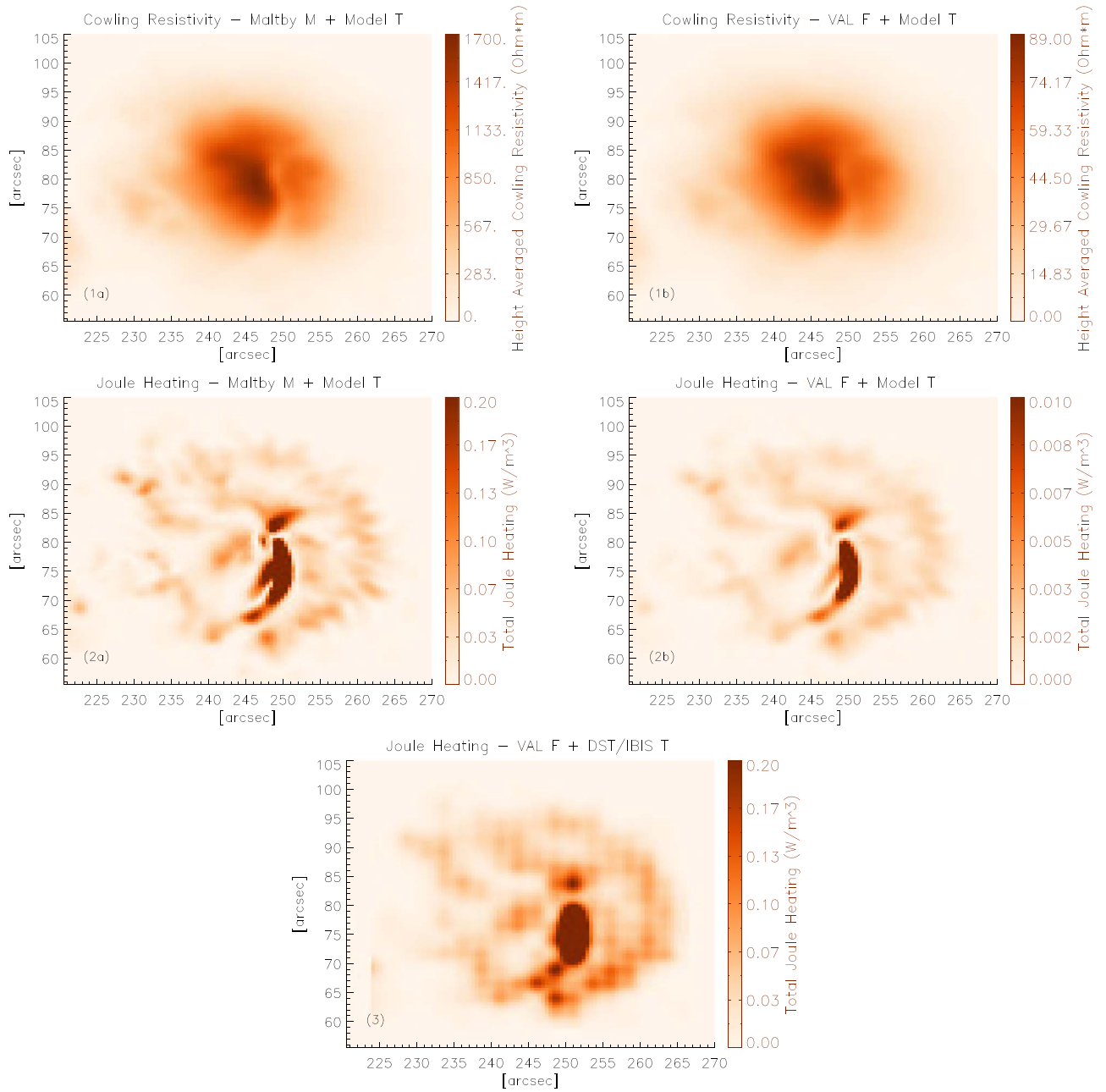


Figure 8. Cowling resistivity (height-averaged between 0 and ~ 1086 km above the photosphere): (1a) Maltby M model with model T ; (1b) VAL F model with model T ; total Joule heating rate between 0 and ~ 1086 km height above the photosphere: (2a) Maltby M model with model T ; (2b) VAL F model with model T ; (3) VAL F model with DST/IBIS T . Gaussian smoothing has been applied to the Joule heating rate with a window of two pixels for the bottom panel. The DST/IBIS and/or SDO/HMI data correspond to AR 12002 at 20:55 UT and 21:00 UT, respectively.

observational data in a consistent way can still yield realistic heating rate values.

4. Conclusions

In this paper, we investigate a mechanism that heats the solar active region atmosphere: Joule heating due to the dissipation of electric currents perpendicular to the magnetic field lines by Cowling resistivity in the chromosphere.

We give an overview of a data-constrained analysis to calculate the Cowling resistivity and the associated Joule heating rate. Our analysis is constrained by both observational data (i.e., magnetic field from NFFF extrapolations applied to SDO/HMI SHARP vector magnetograms, and plasma

temperature from the inversion of spectroscopic data from DST/IBIS using the CAISAR code) and tabulated data from five distinct theoretical/semiempirical solar atmosphere models that were developed to model different regions of the solar atmosphere. We analyze Joule heating over a sunspot umbral LB and demonstrate the consistency of our analysis results while introducing 3D observational temperature data from DST/IBIS, and the effects of the latter on our analysis results. In particular, being able to maintain consistency in our analysis while introducing 3D observational temperature data from DST/IBIS is a major step forward from our last study (Louis et al. 2021). This way, we could also reduce the dependence of our analysis results on theoretical/semiempirical models significantly by constraining the highest two sensitive plasma

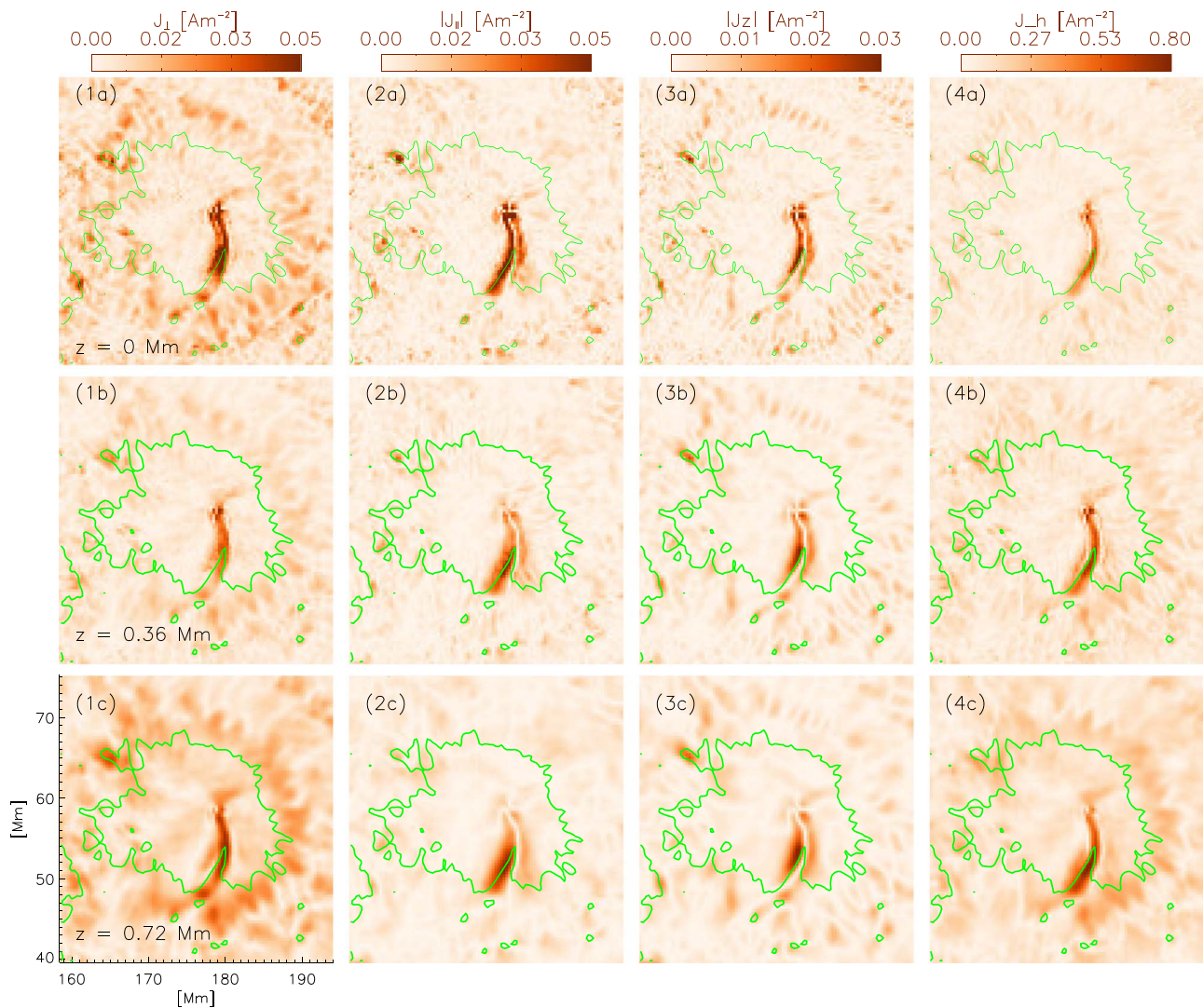


Figure 9. From left to right columns: (1)–(4) perpendicular, parallel, vertical, and horizontal current densities at (top row (a)) the photosphere; (middle row (b)) $z = 0.36$ Mm height above the photosphere; and (bottom row (c)) $z = 0.72$ Mm height above the photosphere in the dashed line box FOV at 20:48 UT on 2014 March 13.

Table 2

Total Joule Heating Rate (W m^{-3}) Values for Each Solar Atmosphere Model with/without DST/IBIS Temperature Data between 0 and ~ 1086 km Height Above the Photosphere on 2014 March 13 at 20:48 UT and 21:00 UT at the Maximum Height-averaged Heating Location on the LB along the White Line, and across the Spine of the Entire LB

Solar Atmosphere Model (with/without DST/IBIS Temperature)	Total Joule Heating Rate between 0 and ~ 1086 km Height above the Photosphere at the Maximum Height-averaged Heating Location on the LB across the White Line (W m^{-3})		Total Joule Heating Rate between 0 and ~ 1086 km Height above the Photosphere across the Spine of the Entire LB (W m^{-3})	
	2014-03-13T20:48 UT	2014-03-13T21:00 UT	2014-03-13T20:48 UT	2014-03-13T21:00 UT
	Maltby M	0.772	0.989	78.83
VAL C	0.049	0.064	5.56	6.16
VAL F	0.021	0.027	2.36	2.61
VAL F with DST/IBIS Temperature	0.597	0.777	91.97	108.04
HSRA	0.09	0.117	10.17	11.26
Ding & Fang	0.884	1.14	94.94	104.56




parameters in our analysis, B and T , by 3D solar chromospheric data based on observations. Our results are encouraging for future use of observational data from different space-borne or ground-based data sources such as NASA's IRIS mission or NSO's DKIST solar telescope to further constrain the plasma parameters in our analysis with high resolution solar chromospheric observational data and hence increase the accuracy of our results.

Acknowledgments

The authors would like to thank the anonymous referee for their valuable comments that improved the quality of this manuscript. They acknowledge support from NSF awards AGS-2020703, AGS-2230633, and AGS-2050340. M.S.Y. and G.P.Z. also acknowledge support from the NSF EPSCoR RII-Track-1 Cooperative Agreements OIA-1655280 and OIA-2148653. M.F. acknowledges support from the NSF REU program under award number AGS-1950831. Any opinions, findings, and conclusions or recommendations expressed in this material are those of the author(s) and do not necessarily reflect the views of the National Science Foundation. A.P. would like to acknowledge the support from the Research Council of Norway through its Centres of Excellence scheme, project number 262622, and Synergy grant No. 810218 459 (ERC-2018-SyG) of the European Research Council. The Dunn Solar Telescope at Sacramento Peak/NM was operated by the National Solar Observatory (NSO). NSO is operated by the Association of Universities for Research in Astronomy (AURA), Inc. under cooperative agreement with the National Science Foundation (NSF). HMI data are courtesy of NASA/SDO and the HMI science team. They are provided by the Joint Science Operations Center—Science Data Processing at Stanford University. IBIS has been designed and constructed by the INAF/Osservatorio Astrofisico di Arcetri with contributions from the Università di Firenze, the Università di Roma Tor Vergata, and upgraded with further contributions from NSO and Queens University Belfast. The “Enhance” code is open source and available at <https://github.com/cdiazbas/enhance>. The authors would like to thank Dr. Rohan E. Louis from Udaipur Solar Observatory in India for providing the inverted temperature data files from DST/IBIS.

ORCID iDs

M. S. Yalim  <https://orcid.org/0000-0002-8496-0353>
 M. Frisse  <https://orcid.org/0009-0002-2773-084X>
 C. Beck  <https://orcid.org/0000-0001-7706-4158>

D. P. Choudhary  <https://orcid.org/0000-0002-9308-3639>
 A. Prasad  <https://orcid.org/0000-0003-0819-464X>
 S. S. Nayak  <https://orcid.org/0000-0002-4241-627X>
 G. P. Zank  <https://orcid.org/0000-0002-4642-6192>

References

- Athay, R. G., & Holzer, T. E. 1982, *ApJ*, 255, 743
 Bahauddin, S. M., Bradshaw, S. J., & Winebarger, A. R. 2021, *NatAs*, 5, 237
 Baso, C. J. D., & Ramos, A. A. 2018, *A&A*, 614, A5
 Beck, C., Choudhary, D. P., Rezaei, R., et al. 2015, *ApJ*, 798, 100
 Beck, C., Gosain, S., & Kiessner, C. 2019, *ApJ*, 878, 60
 Beck, C., Khomenko, E., Rezaei, R., et al. 2009, *A&A*, 507, 453
 Beck, C., Rezaei, R., & Puschmann, K. G. 2012, *A&A*, 544, A46
 Beck, C., Rezaei, R., & Puschmann, K. G. 2013a, *A&A*, 549, A24
 Beck, C., Rezaei, R., & Puschmann, K. G. 2013b, *A&A*, 553, A73
 Beck, C., Rezaei, R., Puschmann, K. G., et al. 2016, *SoPh*, 291, 2281
 Bourdin, P.-A., Bingert, S., & Peter, H. 2014, *PASJ*, 66, S7
 Cavallini, F. 2006, *SoPh*, 236, 415
 Chen, Y., Tian, H., Peter, H., et al. 2019, *ApJL*, 875, L30
 Cowling, T. G. 1957, *Magnetohydrodynamics* (New York: Interscience)
 De Pontieu, B., McIntosh, S. W., Hansteen, V. H., et al. 2009, *ApJL*, 701, L1
 De Pontieu, B., McIntosh, S., Martínez-Sykora, J., et al. 2015, *ApJL*, 799, L12
 Ding, M. D., & Fang, C. 1989, *A&A*, 225, 204
 Gary, G. A. 2001, *SoPh*, 203, 71
 Gingerich, O., Noyes, R. W., Kalkofen, W., et al. 1971, *SoPh*, 18, 347
 Hu, Q., & Dasgupta, B. 2008, *SoPh*, 247, 87
 Hu, Q., Dasgupta, B., & Choudhary, D. P. 2008, *ApJ*, 679, 848
 Hu, Q., Dasgupta, B., DeRosa, M. L., et al. 2010, *JASTP*, 72, 219
 Kalkofen, W. 2007, *ApJ*, 671, 2154
 Khomenko, E. 2017, *PPCF*, 59, 014038
 Leake, J. E., & Arber, T. D. 2006, *A&A*, 450, 805
 Louis, R. E., Beck, C., & Choudhary, D. P. 2020, *ApJ*, 905, 153
 Louis, R. E., Prasad, A., Beck, C., et al. 2021, *A&A*, 652, L4
 Maltby, P., Avrett, E. H., Carlsson, M., et al. 1986, *ApJ*, 306, 284
 Mitra, P. K., Joshi, B., Prasad, A., et al. 2018, *ApJ*, 869, 69
 Narain, U., & Ulmschneider, P. 1996, *SSRv*, 75, 453
 Parker, E. N. 1983, *ApJ*, 264, 635
 Pesnell, W. D., Thompson, B. J., & Chamberlin, P. C. 2012, *SoPh*, 275, 3
 Prasad, A., Bhattacharyya, R., Hu, Q., et al. 2018, *ApJ*, 860, 96
 Priest, E. R., Chitta, L. P., & Syntelis, P. 2018, *ApJL*, 862, L24
 Rezaei, R., & Beck, C. 2015, *A&A*, 582, A104
 Rutten, R. J. 2016, *A&A*, 590, A124
 Sainz Dalda, A. 2017, *ApJ*, 851, 111
 Sakaue, T., & Shibata, K. 2020, *ApJ*, 900, 120
 Schou, J., Scherrer, P. H., Bush, R. I., et al. 2012, *SoPh*, 275, 229
 Solanki, S. K., Lagg, A., Woch, J., et al. 2003, *Natur*, 425, 692
 Syntelis, P., & Priest, E. R. 2020, *ApJ*, 891, 52
 Tritschler, A., Uitenbroek, H., & Reardon, K. 2008, *ApJL*, 686, L45
 Ulmschneider, R., Schmitz, F., Kalkofen, W., et al. 1978, *A&A*, 70, 487
 van Ballegoijen, A. A., Asgari-Targhi, M., Cranmer, S. R., et al. 2011, *ApJ*, 736, 3
 Vernazza, J. E., Avrett, E. H., & Loeser, R. 1981, *ApJS*, 45, 635
 Yalim, M. S., Prasad, A., Pogorelov, N. V., et al. 2020, *ApJL*, 899, L4
 Yalim, M. S., Zank, G., Beck, C., et al. 2023, *J. Phys.: Conf. Ser.*, 2544, 012006